Summer 6-17-2021

Characterization of extracellular vesicles derived from mesenchymal stromal cells by surface-enhanced Raman spectroscopy.

Nina M Ćulum

Tyler T Cooper

Gillian I Bell

David A Hess

François Lagugné-Labarthet

Citation of this paper:
Ćulum, Nina M; Cooper, Tyler T; Bell, Gillian I; Hess, David A; and Lagugné-Labarthet, François, "Characterization of extracellular vesicles derived from mesenchymal stromal cells by surface-enhanced Raman spectroscopy." (2021). *Chemistry Publications*. 254.
https://ir.lib.uwo.ca/chempub/254

Characterization of Extracellular Vesicles Derived from Mesenchymal Stromal Cells by Surface-Enhanced Raman Spectroscopy

Nina M. Ćulum,[1] Tyler T. Cooper,[2] Gillian I. Bell,[2] David A. Hess,[2] François Lagugné-Labarthet[1]*

[1] University of Western Ontario (Western University), Department of Chemistry, 1151 Richmond St., London, Ontario, Canada, N6A 5B7

[2] University of Western Ontario (Western University), Robarts Research Institute, 1151 Richmond St., London, Ontario, Canada, N6A 5B7

* Corresponding author (flagugne@uwo.ca)

Abstract

Extracellular vesicles (EVs) are secreted by all cells into bodily fluids and play an important role in intercellular communication through the transfer of proteins and RNA. There is evidence that EVs specifically released from mesenchymal stromal cells (MSCs) are potent cell-free regenerative agents. However, for MSC EVs to be used in therapeutic practices, there must be a standardized and reproducible method for their characterization. The detection and characterization of EVs is a challenge due to their nanoscale size as well as their molecular heterogeneity. To address this challenge, we have fabricated gold nanohole arrays of varying size and shape by electron beam lithography. These platforms have the dual purpose of trapping single EVs and enhancing their vibrational signature in surface-enhanced Raman spectroscopy (SERS). In this paper, we report SERS spectra for MSC EVs derived from pancreatic tissue (Panc-MSC) and bone marrow (BM-MSC). Using principal component analysis (PCA), we determined that the main compositional differences between these two groups are found at 1236, 761, and 1528 cm^{-1}, corresponding to amide III, tryptophan, and an in-plane -C=C- vibration, respectively. We additionally explored several machine learning approaches to distinguish between BM- and Panc-MSC EVs and achieved 89 % accuracy, 89 % sensitivity, and 88 % specificity using logistic regression.

Keywords

Extracellular vesicles, Surface-enhanced Raman spectroscopy, Nanohole array, Plasmonics, Principal component analysis, Machine learning

Declarations

Funding

This research was supported by the Natural Sciences and Engineering Research Council (NSERC) of Canada (DG RGPIN-2020-06676).

Conflicts of interest/Competing interests

The authors have no relevant financial or non-financial interests to disclose.

Availability of data and material

The data sets generated during and/or analyzed during the current study are available from the corresponding author on reasonable request.

Code availability

Not applicable.

Authors' contributions

Nina M. Ćulum: writing (original draft); investigation (nanofabrication and sample characterization); formal analysis; conceptualization.

Gillian I. Bell: investigation (sample isolation and collection).

Tyler T. Cooper: investigation (sample isolation and collectionn).

David A. Hess: supervision; conceptualization.

François Lagugné-Labarthet: supervision; writing (review and editing); conceptualization.

Ethics approval

Not applicable.

Consent to participate

Not applicable.

Consent for publication

All authors have given approval of the final version of the manuscript.

Introduction

Extracellular vesicles (EVs) are a highly complex group of membrane-bound vesicles released by all cells into bodily fluids such as saliva, plasma, milk, and urine [1]. EVs are divided into three sub-classes based on their size, biogenesis, and differences in molecular content [2]. Apoptotic bodies, ranging in diameter from 1 – 5 μm, are formed during the late stages of apoptosis and typically contain cytoplasmic organelles and genetic material [3, 4]. Smaller vesicles, exosomes and microvesicles (diameter ranging from 30 – 150 nm and 100 – 1000 nm, respectively), are of particular interest to researchers due to their involvement in intercellular signalling and communication through the transfer of proteins and RNA [5, 6]. Researchers aiming to develop methods for non-invasive and early stage disease detection, primarily in cancer research, have focused their attention on EVs as they contain biomarkers reflective of their parent cell [7, 8]. Not as extensively researched, however, are the regenerative and therapeutic applications of EVs [9, 10].

Mesenchymal stromal cells (MSCs) have been shown to induce cellular changes in nearby cells through the release of chemical messengers, known as paracrine signalling, particularly via their secreted EVs [11]. EVs released from MSCs are potent cell-free regenerative and restorative agents that are effective in neural [12, 13, 14], myocardial [15, 16, 17], hepatic [18, 19], renal [20, 21, 22], cutaneous [23, 24, 25], skeletal [26, 27], cartilage [28, 29], and muscular regeneration [30, 31]. In particular, MSCs derived from bone marrow (BM-MSC) have been widely studied due to the regenerative potential of their secreted EVs. For example, BM-MSC EVs have been shown to reduce neuroinflammation in traumatic brain injuries [32], promote survival of retinal ganglion cells and the regeneration of their axons [33], suppress inflammation response in acute myocardial infarction [34], and promote proliferation of cisplatin-damaged proximal tubular epithelial cells

[35]. However, to be used in therapeutic and regenerative practices, sensitive and reproducible characterization protocols must be established. The characterization of EVs is challenged by their nanoscale size (30 – 150 nm for exosomes and 100 – 1000 nm for microvesicles) and heterogeneity in terms of size range, morphology, molecular composition, and biogenic mechanisms [3, 36, 37].

Plasmon-enhanced spectroscopies are promising techniques for the detection and characterization of nanoscale biological samples such as EVs. Surface-enhanced Raman spectroscopy (SERS) is a plasmon-based, non-destructive, and label-free technique capable of single-molecule detection [38, 39]. The same chemical information is gathered as in traditional Raman spectroscopy, but with greatly enhanced signal. There are two general methods of EV capture for SERS analysis: immunoaffinity-based methods and size-based methods [40]. In the immunoaffinity-based approach, EVs are specifically captured based on the surface proteins they are known to express, either by antibody-functionalized SERS probes [41, 42] or antibody arrays [43, 44]. The largest disadvantage to this method is the suppression of some EV signals in a given sample since EVs are known to be molecularly heterogeneous, as shown by Kim *et al* [45]. To work around this, the authors instead functionalized their SERS substrates with varying types of self-assembled monolayers. A simpler approach to capturing EVs without eliminating some of their signals is the size-based capture method, which aims to trap single EVs. Smaller EVs (typically < 1000 nm in diameter) are targeted while larger particles are excluded. Examples of such SERS substrates include nanobowls [46], nanorods [47], and nanopyramids [48].

In this proof-of-concept study, we have investigated EVs derived BM-MSCs as well as MSCs derived from pancreatic tissue (Panc-MSC) by SERS. While SERS has been extensively used in the characterization of tumour-derived EVs, its application in the characterization of MSC EVs has been largely underexplored. Although BM-MSC EVs have been characterized by Raman spectroscopy, none to date to our knowledge have been characterized using SERS [49, 50]. Previous preliminary work reported from our group has demonstrated the feasibility of using these platforms for SERS characterization of Panc-MSC EVs, but a small sample size was reported [51]. Herein, we have built on these concepts and further explored the capacity of these nanohole arrays to trap, detect, and differentiate EVs from these two sources. We have fabricated plasmonically active gold nanohole arrays of varying size (100 – 1000 nm) and shape (circles, squares, and triangles) by electron-beam lithography (EBL) that are capable of EV trapping and signal enhancement for SERS. This paper reports spectral fingerprints associated with both EV sources, and is the first to report SERS spectra of BM-MSC EVs. Additionally, we have determined the main compositional differences between Panc-MSC and BM-MSC EVs using principal component analysis (PCA) and employed machine learning algorithms to differentiate the two groups with high accuracy, sensitivity, and specificity.

Experimental

Electron-beam lithography (EBL)

Nanohole arrays were fabricated using the protocol established by Kaufman *et al* [51]. A negative-tone resist, ma-N 2405 (Microchem), was spin-coated onto reactive O_2-cleaned glass coverslips at 3000 rpm for 45 seconds, corresponding to a thickness of approximately 500 ± 50 nm, then baked at 90 °C for 90 seconds. AquaSAVE^{TM} conductive polymer (Sigma-Aldrich) was then spin coated at 1000 rpm for 45 seconds and baked at 90 °C for 45 seconds. EBL and scanning electron microscopy (SEM) imaging were performed using a LEO 1530 scanning electron microscope (Zeiss) with a 30.0 kV EHT voltage, 10.0 μm aperture, and 30.0 – 50.0 pA current. Arrays of varying shape (square, circle, and triangle) and size (0.1 – 1.0 μm in 0.1 μm increments, 1.0 μm width between holes) were written using ELPHY Quantum software (Raith Nanofabrication). All patches measured 50 × 50 μm^2. Following beam exposure, substrates were soaked in DI water to remove the conductive layer. Samples were developed in MF-319 (MicroChem) for 40 seconds, soaked in DI water, and air dried to avoid collapsing the nanopillars. Samples were subjected to an O_2 plasma descum process (Trion Technology) for 60 seconds to remove residual resist surrounding the nanopillars. A 3 nm adhesion layer of titanium was then deposited onto the samples followed by 30 nm of gold by electron beam evaporation (Angstrom Engineering). For lift-off, samples were exposed to Remover-PG (MicroChem) heated to 80 °C for 2 hours. Remover-PG was removed from the samples by soaking in a 1:3 solution of methyl isobutyl ketone (MIBK) and isopropanol (IPA). Samples were then rinsed with IPA and dried under N_2. For final cleaning, samples were immersed in Nano-Strip® (Cyantek) heated to 80 °C for 30 minutes, then DI water for 15 minutes, and dried under N_2. Finally, samples were again subjected to O_2 plasma for 5 minutes to remove any remaining resist from the holes.

Visible-near infrared (Vis-NIR) absorption measurements

Absorption spectra of gold nanohole arrays were obtained with a homebuilt setup consisting of an HL-2000 halogen lamp (Ocean Optics), which covers a spectral range of about 400 – 1000 nm, coupled to an inverted optical microscope by a 100 μm optical fibre. The source beam was first expanded by a 10 × objective (N.A. = 0.25), recollimated using 20 × objective (N.A. = 0.40), and finally collected by a 20 × objective (N.A. = 0.50). The resulting spot sizes were approximately 50 μm in diameter, covering the surface of a single array. Scattered light was then analysed with a USB 4000-Vis-NIR-ES spectrometer (Ocean Optics).

Cell culturing

Human bone marrow aspirates were obtained from healthy donors with informed consent from the London Health Sciences Centre (London, ON). BM-MSCs were established and cultured in AmnioMax-C100™ media with AmnioMax™ C100 supplement (Life Technologies) as previously described by Sherman *et al* [52]. Ricordi-chamber isolated human islets were obtained through the Integrated Islet Distribution Program (USA) for the establishment of Panc-MSCs as previously described by Cooper *et al* [53]. 200 islet equivalents were plated in RPMI 1640 + 10% fetal bovine serum (FBS) for up to 7 days. Between 5 – 7 days, adherent fibroblast-like cells were separated from non-adherent islets by media aspiration followed by trypzination and filtration using a 40 µm cell strainer. Single cell suspensions were subsequently reseeded on tissue culture plastic at 4000 cells/cm^2 and expanded in Amniomax-C100™ with AmnioMax™ E100 supplement (Life Technologies).

Extracellular vesicle (EV) isolation

EVs were isolated by ultrafiltration as previously described by Cooper *et al* [54]. Conditioned media (CM) was generated by culturing BM-MSC and Panc-MSC to ~80% confluency, rinsed 3 times with pre-warmed phosphate buffer solution (PBS), and switched to basal AmnioMax™ C100 media (Life Technologies) without supplement. Media was collected after 24 hours of cell culture. Cell debris were removed by centrifugation for 10 minutes at 600 × *g*. Cell-free CM was concentrated by centrifugation in 100 kDa centrifuge filter units for 20 minutes at 2800 × *g*. 20 mL was concentrated in a single unit, requiring two centrifugations, producing a final volume of 120 µL. After the second centrifugation, 10 mL of 0.22 µm-filtered PBS was used to wash out residual phenols, proteins, and salts. EV samples were collected and placed into Eppendorf tubes and stored at -20 °C for up to 1 month.

Atomic force microscopy (AFM)

Purified EV solutions were diluted (1:20) in Milli-Q water. 10 µL of the dilute EV samples were drop-casted onto chemically cleaned glass coverslips (22 mm × 22 mm × 0.15 mm) and dried overnight in a biological safety cabinet. Scans were obtained using a BioScope Catalyst atomic force microscope (Bruker). NCLR-50 Silicon probes (Nanoworld) with a force constant of 48 N/m and a resonance frequency of 190 kHz were employed under tapping mode. Height images were recorded at 256 × 256 pixels and a scan rate of 0.50 Hz. Imaging processing was subsequently performed using Gwyddion software.

Surface-enhanced Raman spectroscopy (SERS)

Concentrated EV samples were diluted 1:20 with Milli-Q water. 10 – 20 µL of dilute EV samples were drop-cast onto nanohole arrays. EV-water solution was removed from the array using cohesive properties allowed by a Kimwipe absorbent paper (Kimberly-Clark Inc.). The edge of the absorbent paper was placed on the corner of the solution droplet, allowing solution removal via capillary action. This capillary flow also induces EVs to locate and stay in the nanoholes. Lastly, EV solutions were allowed to dry for 15 – 30 minutes prior to SERS measurements. SERS spectra presented in **Fig. 4** were acquired with a LabRAM HR spectrometer (Horiba Scientific) using a 632.8 nm excitation laser source, 600 grooves/mm grating, 100 × objective (N.A. = 0.9), and 200 µm pinhole. Laser power was set to 2.5 mW with an acquisition time of 60 seconds per spectrum. SERS spectra presented in **Fig. 5** and **Fig. S2** were extracted from SERS maps that were acquired with an XploRA^{TM} PLUS spectrometer (Horiba Scientific) using a 785 nm excitation laser source, 600 grooves/mm grating, 100 × objective (N.A. = 0.9), and 100 µm pinhole. Laser power was set to 5 mW with an acquisition time of 4 seconds per spectrum.

Statistical analysis and machine learning

Principal component analysis (PCA) was performed to reduce the dimensionality of the spectral data and to determine the peaks responsible for the most variance between the two EV sources. All spectra were normalized prior to PCA. The first 19 principal components (PCs) were selected to explain 98% of variance among spectra. After score plots were constructed, 95% confidence ellipses were fitted around each cluster type. The first 19 PCs were then used as input data for five different machine learning algorithms: logistic regression, support vector machine, random forest, Naïve Bayes, and CN2 rule induction. In each machine learning case, models were tested using leave-one-out cross validation. PCA and machine learning were performed using Orange software (version 3.27.1).

Results and discussion

Nanohole array fabrication and characterization

Electron-beam lithography (EBL) is a nanofabrication technique used to create nanostructures with 20 nm spatial resolution. Nanostructures are fabricated by scanning a focused beam of electrons from an SEM microscope onto an electron-sensitive photoresist, which undergoes chemical changes in exposed areas. The EBL nanofabrication process is illustrated in **Fig. 1A**. Some substrates, such as the glass coverslips used here, additionally require the application of a conductive layer on top of the resist to prevent charging on the substrate surface during the inscription of the pattern, which minimizes the loss of resolution when the substrate is exposed to the electron beam. Following exposure, the substrate is developed in a chemical bath to remove some of the resist and reveal the desired pattern. For the purpose of fabricating nanohole arrays, a negative-tone resist is desired, and ma-N 2405 was used. Negative-tone resists undergo cross-linking in exposed areas, and non-exposed regions are removed during development, thus producing the reverse or “negative” image of the final pattern. For nanohole arrays, this “negative” image translates to nanopillar arrays (**Fig. 1B**). Since the objective of the work is to use the nanohole arrays in SERS sensing, metals must be deposited onto the developed substrate for the propagation of plasmons. Gold was selected for these experiments due to its greater stability in air compared to other common SERS-active metals such as silver and copper. Finally, the metallic substrate is placed into a chemical bath to remove any remaining resist and reveal the final nanoholes in a process called lift-off (**Fig. 1C**).

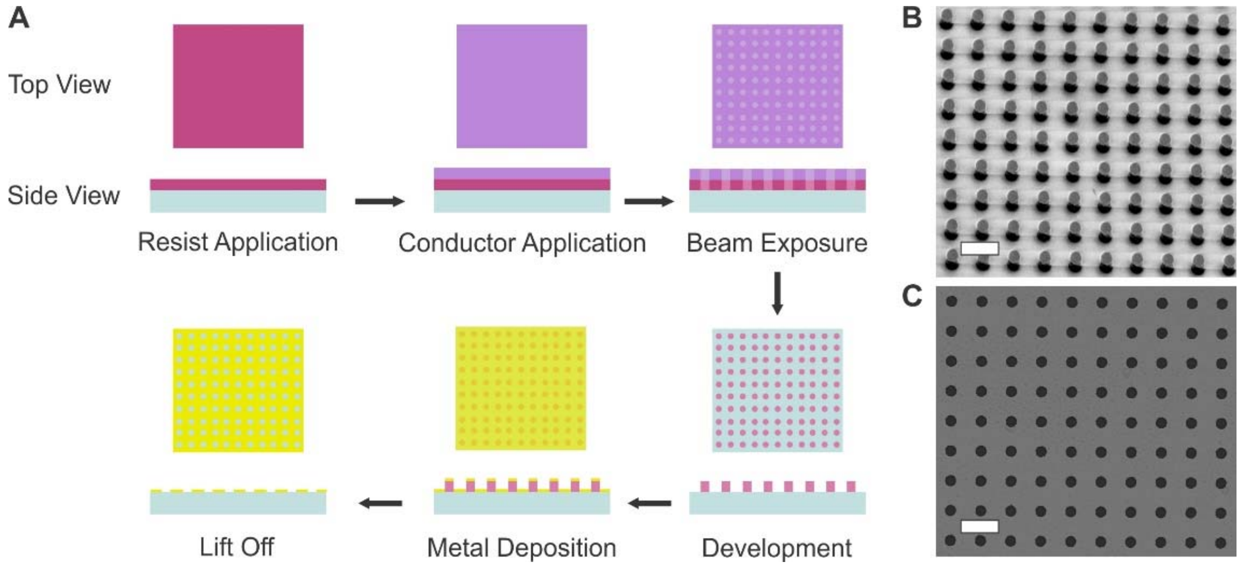

Fig. 1 Schematic illustration of nanohole array fabrication by EBL using a negative-tone resist **(A)**, with example SEM images of 700 nm circular arrays before lift-off **(B)** and after lift-off **(C)** (scale bars = 2 μm)

Gold nanohole arrays of varying size (100 – 1000 nm) and shape were fabricated by EBL, imaged by SEM, and characterized by vis-NIR spectroscopy. Shapes explored for these arrays consisted of triangles (**Fig. 2A, D**), squares (**Fig. 2B, E**), and circles (**Fig. 2C, F**). Fallen nanopillars or nanocaps are visible on the smaller-sized arrays (**Fig. 2D-F**) and not on the larger-sized arrays (**Fig. 2A-C**) since negative resists become increasingly difficult to remove as hole size decreases. Nevertheless, smaller arrays are still suitable for EV capture if the nanocaps do not collapse directly into the holes. Absorption measurements were subsequently performed to determine the position of their plasmonic resonances, as shown on the triangular arrays (**Fig. 2G, S1**). Two resonance wavelengths are observed: one around 650 – 690 nm, and another around 750 – 780 nm. Similar results were observed with the circular and square arrays, and is consistent with the results previously reported [51]. When the excitation wavelength matches their resonance wavelengths (i.e., 633 and 785 nm), the conduction electrons at the metal surface of the arrays are driven to collective oscillation at a frequency referred to as the localized surface plasmon resonance (LSPR) [55]. The higher energy band around 650 – 690 nm is generally referred to as the quadrupolar resonance, while the lower energy band around 750 – 780 nm is referred to as the dipolar resonance. Consequently, large enhancements of the local electromagnetic fields of radiation are confined at the vicinity of the nanoholes. Since the EVs are smaller in diameter compared to the hole sizes, we expect EVs to be captured by the nanoholes and their Raman signals to be enhanced as a result.

The trapping capabilities of these nanohole arrays has been previously published by our group, both by polystyrene beads as proof-of-concept, as well as with EVs themselves [51]. Trapping of the EVs is enabled by the flow of the EV-containing solution and the size match between the EVs and the nanohole cusps. However, trapping of small EVs cannot be observed optically due to the diffraction limited spatial resolution of our optical measurement. Therefore, blind SERS mapping over large areas of the nanohole arrays is necessary to reveal which holes are filled with one or more EVs (areas with signal) and which holes are empty (areas without signal). SERS mapping experiments showed that approximately 12 % of the holes were occupied by one or more EVs (**Fig. S2**). For SERS of EVs, the circular arrays were the least preferential due to a lower throughput from the EBL process compared to the triangular and square arrays. This lower throughput could potentially be due to the fact that the corners of the triangles and squares provided more anchoring points for the pillars with three and four points, respectively. Conversely, the highest throughput of arrays was achieved with the square arrays, allowing more opportunity for the square arrays to capture EVs. Therefore, square arrays were generally preferred for SERS experiments. By utilizing these SERS platforms in conjunction with lasers of excitation wavelengths that match their LSPRs, we are able to study samples with inherently weak Raman signals without the need to increase laser power or accumulation time, which is likely to burn the samples, or the need to use a higher energy laser wavelength (i.e., green laser), which is likely to induce high background fluorescence [56].

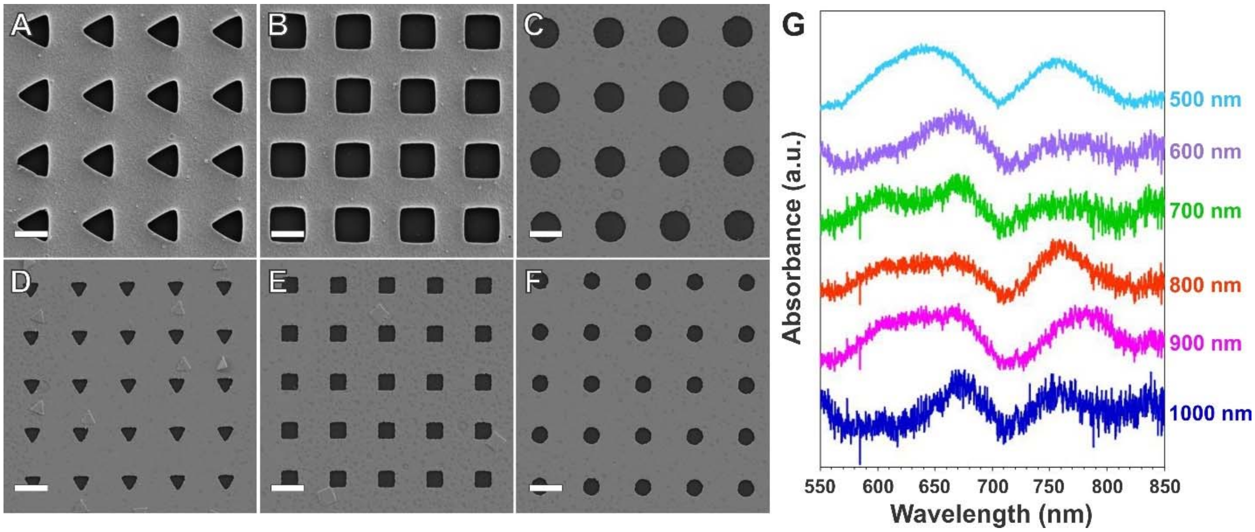

Fig. 2 SEM images of 1000 nm triangular **(A)**, square **(B)**, and circular arrays **(C)**, and 500 nm triangular **(D)**, square **(E)**, and circular arrays **(F)** (scale bars = 1 µm); background-corrected absorption spectra of 500 – 1000 nm triangular arrays **(G)**. Original absorption spectra are presented in **Fig. S1**

EV characterization

AFM was employed for EV imaging and height quantification since it causes minimal deformations to the soft EV surface when scanning in tapping mode. For AFM imaging, dilute solutions of EVs were drop-casted on clean glass coverslips and allowed to dry. AFM scans of EVs isolated from both Panc-MSC (**Fig. 3A**) and BM-MSC (**Fig. 3C**) revealed small, quasi-spherical objects on the substrate surface. A cross-section of one of these features is shown in **Fig. 3B**. The average height of the adhered EVs from the Panc-MSC samples measured over 106 individual EVs was 210 ± 40 nm, with the size distribution ranging from 110 – 330 nm (**Fig. 3D**). Similarly, the average height of the adhered EVs from the BM-MSC samples was 190 ± 50 nm, with a size distribution of 50 – 300 nm. Recalling that microvesicles range in diameter from 100 – 1000 nm, these distributions are well within the accepted EV size range.

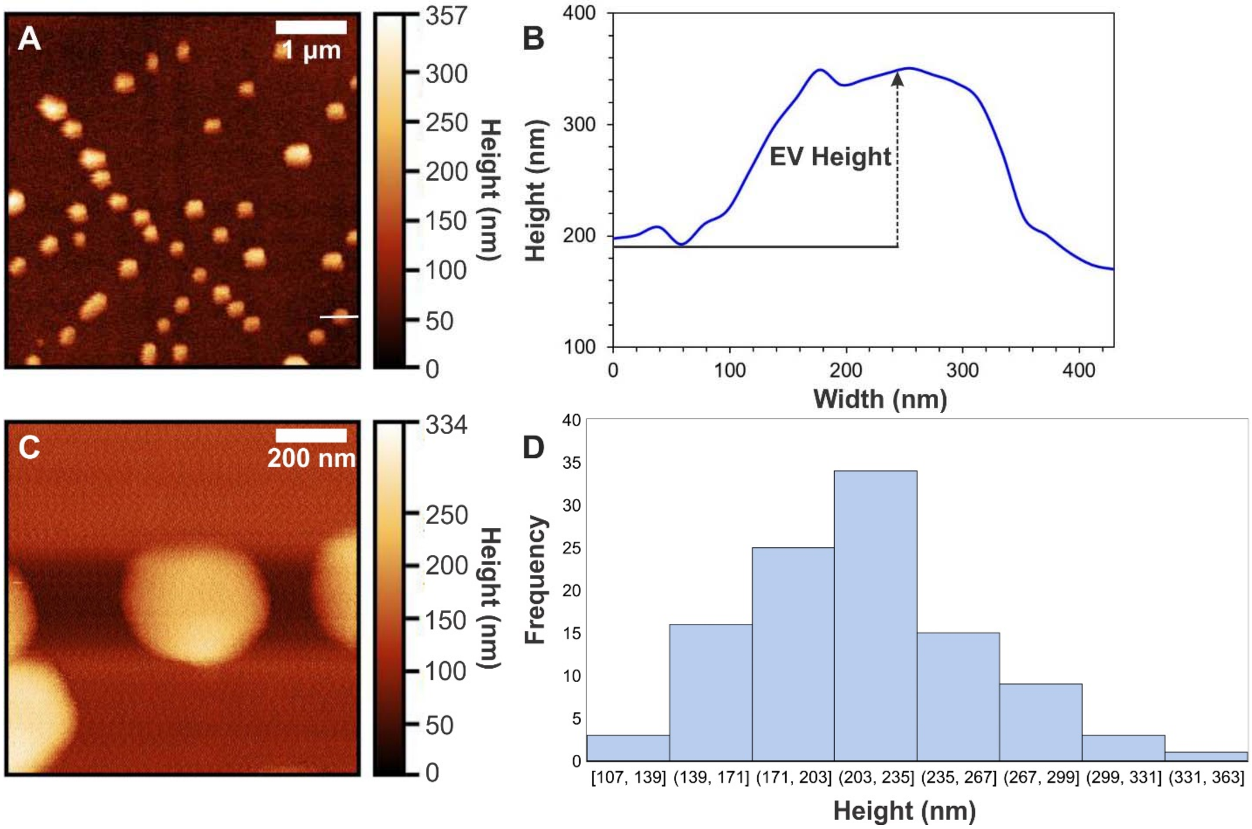

Fig. 3 (5 × 5) µm^2 AFM scan of Panc-MSC EVs on a bare glass coverslip **(A)** and the cross-section of a single EV **(B)**, as indicated by the white line in **(A)**; (1 × 1) µm^2 AFM scan of an individual

BM-MSC EV on a bare glass coverslip **(C)**; histogram representing the height distribution of a Panc-MSC sample containing 106 EVs **(D)**

Initial SERS characterization of EVs from the Panc-MSC sample was conducted with an excitation wavelength set at 632.8 nm, which utilizes the quadrupolar resonance of the nanohole arrays. Spectra were acquired by focusing a 632.8 nm laser with a 100 × objective (N.A. = 0.90) on holes presumably containing EVs, and a background spectrum was recorded by focusing the same laser off the array on flat gold. The resulting spectra of three individual EVs reveal an abundance of peaks in the 700 – 1800 cm^{-1} fingerprint region, as expected since this is a significant Raman spectral window for biological samples, whereas none are visible in the background spectrum (**Fig. 4**). Since the LSPR decays exponentially away from the platform surface, the effective sensing zone of the plasmonic arrays is confined within the first 10 – 20 nm away from the metal surface [57]. Since plasma membranes are typically about 5 nm thick, we expect to detect not only the SERS signals of the surface content of the EVs (i.e., surface proteins and lipids), but also the SERS signals of their cargo (i.e., proteins and genetic material). The analysis of the collected spectra showed that some Raman modes are common among the three EVs, which are summarized in **Table 1**. Protein peaks are observed at 1052 cm^{-1} and 1242 cm^{-1} which can be assigned to C-O/C-N stretching and amide III, respectively. Additionally, amino acid peaks are present at 1210 cm^{-1}, which are attributed to tyrosine and phenylalanine and 1580 cm^{-1}, corresponding to phenylalanine. Nucleic acid peaks are present at 791 cm^{-1} and 1509 cm^{-1}, corresponding to pyrimidines and adenine/cytosine, respectively. The peak present at 1308 cm^{-1} can be attributed to the CH_2/CH_3 twisting, bending, or wagging in lipids or collagen. Although these peaks are found in common by a couple of spectra, there is still variety in the spectra in terms of peak positions and intensities, which can be attributed to the molecular heterogeneity of EVs.

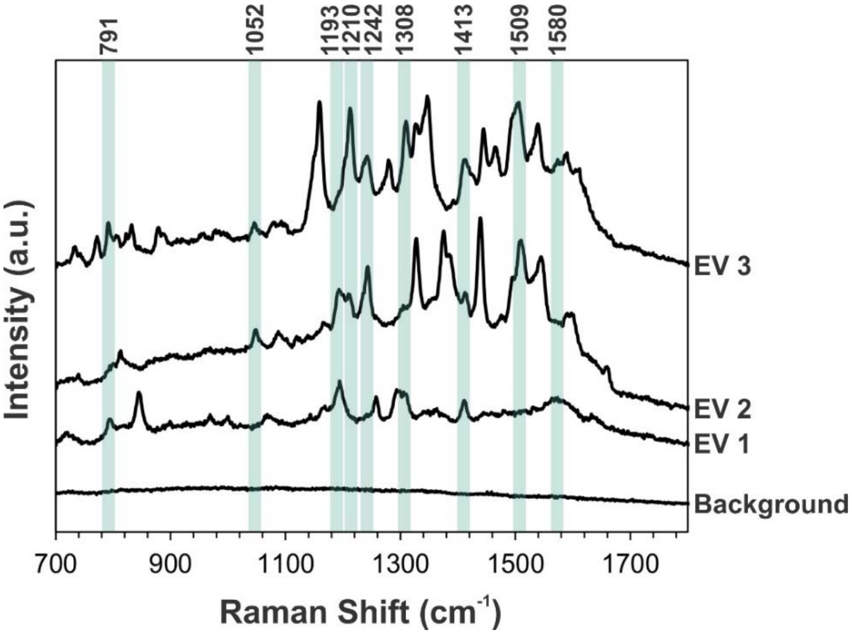

Fig. 4 Three SERS spectra of Panc-MSC EVs acquired with a 632.8 nm laser with a background spectrum for comparison and common peaks highlighted in blue

Table 1 Assignments of common peaks shared among Panc-MSC EV spectra from **Fig. 4**

Peak (cm^{-1})	Presumed Origin	Ref. Peak (cm^{-1})	Ref.
791	Pyrimidine	791	[58]
1052	C-O/C-N stretch in proteins	1053	[58]
1193	Ring stretch, CH bend, CH_2 twist	1194	[59]
1210	C-C_6H_5 stretch in tyrosine and phenylalanine	1210	[58]
1242	Amide III	1243	[58, 60]
1308	CH_2/CH_3 twisting, bending, and wagging in lipids or collagen	1308	[58]
1413	Ring stretch	1412	[58]
1509	Ring breathing mode of adenine and cytosine	1510	[58]
1580	C-C stretch and C=C bend of phenylalanine	1580	[58]

While we were able to collect spectra for the Panc-MSC EVs at 632.8 nm, the spectral acquisition for the BM-MSC EVs was unsuccessful at the same wavelength due to the presence of a fluorescence background. To mitigate the background fluorescence, we switched to a 785 nm laser, thus exploiting the dipolar resonance of the nanohole arrays. Data sets for Panc-MSC and BM-MSC EVs comprised of 25 and 19 SERS spectra, respectively, were obtained with a 785 nm excitation laser source. Since EVs of this size are not visible with an optical microscope, we located EVs on the nanohole arrays by mapping areas approximately $(10 \times 10)\ \mu m^2$ in size. Similarly to the Panc-MSC results obtained with the 632.8 nm laser, the spectra corresponding to Panc-MSC (**Fig. 5A**) and BM-MSC (**Fig. 5B**) EVs vary considerably, but common peaks within each data set can still be identified. These common peaks are summarized in **Table 2**. Regarding the SERS spectra of the Panc-MSC EVs (**Fig. 5A**), protein peaks are identifiable at 813 cm^{-1} and 1151 cm^{-1}, corresponding to C-C and C-N stretching, respectively. Additionally, the peak at 1274 cm^{-1} belongs to amide III. Many amino acid peaks are located at 761 cm^{-1} (tryptophan), 873 cm^{-1} (hydroxyproline, tryptophan), 1206 cm^{-1} (hydroxyproline, tyrosine), and 1364 cm^{-1} (tryptophan). Lastly, the peak at 1334 cm^{-1} can be attributed to CH_2/CH_3 twisting, bending, or wagging in collagen or nucleic acids. Interestingly, there are far less peaks attributable to nucleic acids for the Panc-MSC EV spectra obtained with the 785 nm laser compared to those obtained with the 632.8 nm laser, and far more attributable to proteins and amino acids. The spectral differences between Panc-MSC EVs acquired with the 632.8 nm and 785 nm lasers could be explained by EV rupturing due to differences in laser energy, since the 632.8 nm excitation wavelength used to collect the spectra in **Fig. 4** is higher in energy compared to the 785 nm excitation wavelength used to collect the spectra in **Fig. 5A**. Additionally, the spectra presented in **Fig. 4** were gathered with longer acquisition times than the spectra presented in **Fig. 5A**, at 60 and 4 seconds, respectively. Although not specific to EVs, targeted laser-induced cell lysis, or the breakdown of the cell membrane, has been demonstrated, and a similar process could be unfolding here [61, 62]. Since genetic material carried in EVs is contained by a membrane typically decorated with surface proteins, we might expect to see more protein signals compared to nucleic acid signals when the membrane is intact. Regarding the SERS spectra of the BM-MSC EV (**Fig. 5B**), many protein peaks are also visible at 866 cm^{-1}, 1158 cm^{-1}, 1236 cm^{-1}, 1265 cm^{-1}, and 1658 cm^{-1}. A few nucleic acid peaks can be additionally seen at 803 cm^{-1} (uracil), 1480 cm^{-1} (guanine and adenine), and 1612 cm^{-1} (cytosine). A lipid peak can also be found at 1077 cm^{-1}, corresponding to a C-C/C-O stretch.

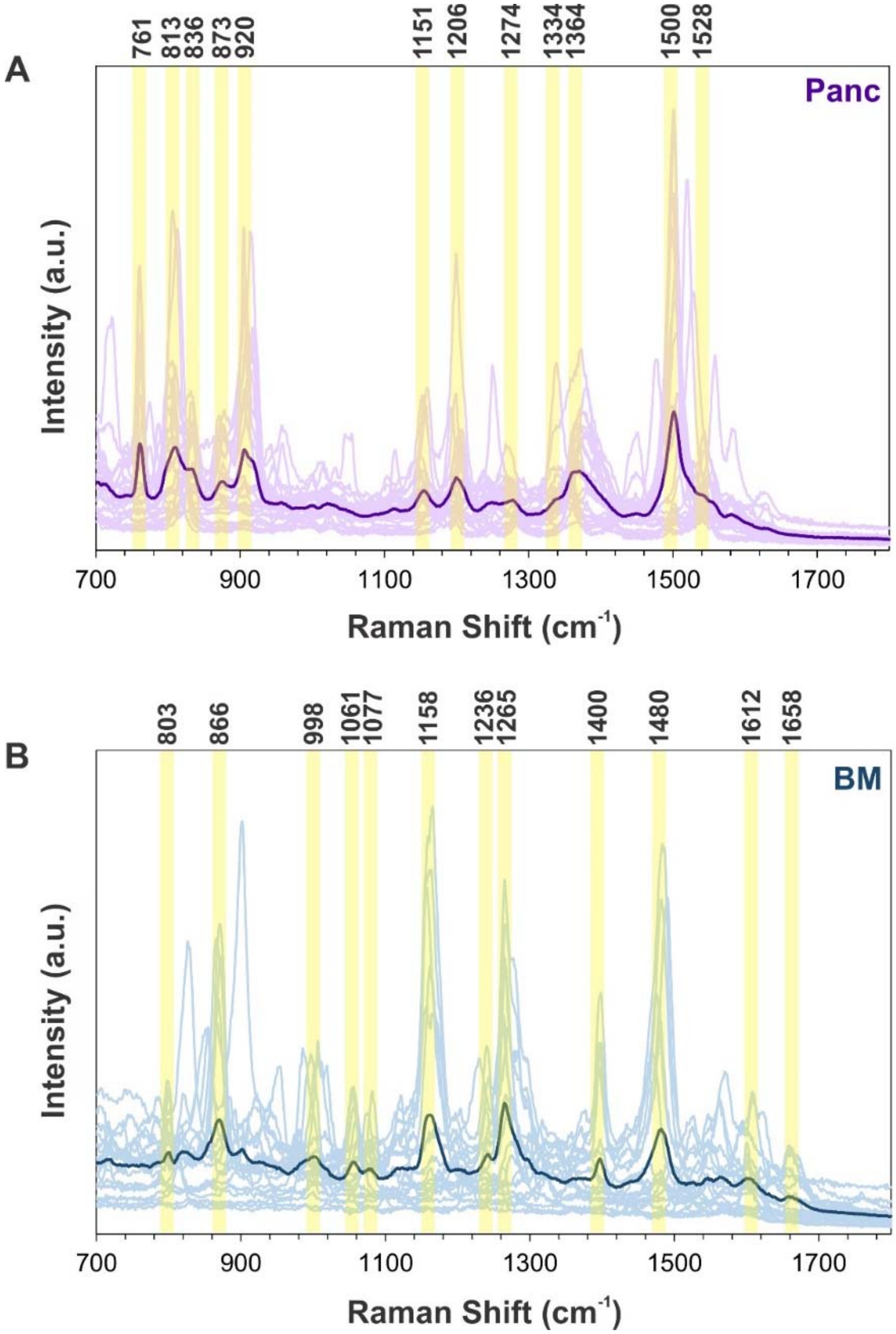

Fig. 5 SERS spectra of Panc-MSC EVs **(A)** and BM-MSC EVs **(B)** acquired with a 785 nm laser, where individual spectra are represented by lighter lines, average spectra are represented by darker lines, and common spectral peaks are highlighted in yellow

Table 2 Assignments of common peaks shared among BM-MSC and Panc-MSC EV spectra from **Fig. 5**

Peak (cm^{-1})	BM	Panc	Presumed Origin	Ref. Peak (cm^{-1})	Ref.
761		x	Ring breathing in tryptophan	760	[58]
803	x		Ring breathing mode in uracil	802	[58]
813		x	C-C stretch in collagen	813	[58]
836		x	Deformative vibrations of amine groups	838	[58]
866	x		C-C stretch in collagen	868	[59]
873		x	Hydroxyproline, tryptophan	873	[58]
920		x	C-C stretch of proline ring/glucose/lactic acid; collagen assignment	920	[58]
998	x		C-O in ribose, C-C	996	[49, 58]
1061	x		C-C in-plane bending; C-N stretching	1053	[58]
1077	x		C-C or C-O stretch in lipids	1078	[63]
1151		x	C-N stretch in proteins	1152	[58, 63]
1158	x		C-C/C-N stretch in proteins	1158	[58]
1206		x	Hydroxyproline, tyrosine (collagen assignment)	1206	[58]
1236	x		Amide III	1235	[58]
1265	x		Amide III (collagen assignment)	1265	[63]
1274		x	Amide III	1275	[58]
1334		x	CH_2CH_3 twisting and wagging in collagen and nucleic acids	1335	[58, 63]
1364		x	Tryptophan	1365	[58]
1400	x		N-H in-plane deformation	1400	[58]
1480	x		Ring breathing mode in guanine and adenine	1485	[58]

1500		x	N-H bending	1506	[58]
1528		x	In-plane vibrations of -C=C-	1528	[60]
1612	x		Cytosine (NH_2)	1610	[58]
1658	x		Amide I (α-helix)	1658	[58]

Statistical analysis and machine learning

Principal component analysis (PCA) was employed to reduce the dimensionality of the spectral data sets and to determine the main compositional differences between the Panc-MSC and BM-MSC EVs. In PCA, complex data sets can be transformed to smaller data sets, or principal components (PCs), that contain most of the information of the original data. Maximum information, or explained variance, is put into the first PC, and each subsequent PC accounts for less explained variance until 100 % of the original data is accounted for. With respect to the spectra presented in **Fig. 5**, the first principal component (PC1) that explains 50.7% of variance corresponds to a protein peak at 1236 cm^{-1}, which belongs to amide III. The second principal component (PC2) that explains 15.5% of variance corresponds to an amino acid peak at 761 cm^{-1}, which corresponds to tryptophan. However, plotting PC1 *versus* PC2 reveals a large overlap in data between the two groups, limiting the ability to separate the two EV types (**Fig. 6A**). We additionally plotted PC1 *versus* the third principal component (PC3), which accounts for 7.7% of variance and corresponds to a peak at 1528 cm^{-1} (in-plane -C=C- vibrations). In the second score plot, both data sets are clustered more tightly compared to the first score plot, as evidenced by the smaller confidence ellipses surrounding the former compared to the latter (**Fig. 6B**). However, there was still a great amount of overlap between the two ellipses, and we could only classify the two EV groups with 82% accuracy, 74 % sensitivity, and 84 % specificity. It is not uncommon for PCA to perform poorly in terms of classification tasks since PCA ignores class labels while attempting to maximize variance, and often PCA is used in conjugation with other classification techniques to improve class separability [64]. To mitigate this problem, we used the PC scores as classifiers in various machine learning algorithms. Machine learning is a powerful and automatized technique that can be used to make predictions about data without being explicitly programmed for these tasks. Treating spectral data sets with PCA is favoured when exploring classification techniques by machine learning since smaller data sets are less computationally demanding for machine learning algorithms, and therefore faster. Furthermore, feeding raw spectral data to a machine learning algorithm can lead to overfitting due to the high dimensionality of the data [65]. Machine learning algorithms in conjunction with the PCA data obtained were thus explored to increase class separation between the BM- and Panc-MSC EV spectral data as well as classification accuracy.

Five different machine learning algorithms were employed: random forest (RF), support vector machine (SVM), Naïve Bayes (NB), CN2 induction (CN2), and logistic regression (LR). RF is a technique that includes an ensemble of decision trees, in which data are modeled in hierarchical structures by a series of if/else statements [66, 67]. SVM creates an optimal separating line for the classification of all the input data into different classes, while NB is a statistical method that computes the probability of an input's relevance to a pre-defined class [67]. In rule induction systems such as CN2, rules are created that fit the example cases, and solutions are found by linking rules to known facts (i.e., the data set) [68]. Lastly, LR calculates the probability of class membership based on the sigmoid or logistic function [69]. Each model was tested using leave-one-out cross validation (LOOCV) to minimize bias that could occur when training with a small sample size. In the LOOCV procedure, one spectrum is held as a test sample while the remaining 43 spectra are used to train the model, until each spectrum as been used as a test sample once. By visualizing the output scores, we observed that RF could not significantly separate the two groups of EVs, while NB and LR performed the best in terms of class separation (**Fig. 6C**). To further assess the models, we plotted receiver operating characteristic (ROC) curves and determined the area under the curves (AUCs). While all five models had high, AUC values, NB, RF, and LR outperformed CN2 and SVM with AUC values of 0.901, 0.921, and 0.926, respectively, compared to 0.866 and 0.891 (**Fig. 6D**). Since AUC values are quite close together, it is necessary to also compare the models in terms of classification accuracy, sensitivity, and specificity (**Table 3**). CN2 had an unfavourable accuracy of 80 %, which was even lower than the accuracy achieved using PCA only. SVM, RF, and NB performed marginally better than PCA only with accuracies of 84 % each. LR was able to achieve a high accuracy of 89 %, as well as a high sensitivity and specificity of 89 and 88 %, respectively. While all five machine learning algorithms performed well in terms of differentiating the Panc- and BM-MSC EVs, LR is the most favourable approach for this data set, considering the high AUC, accuracy, sensitivity, and specificity achieved compared to the four other algorithms.

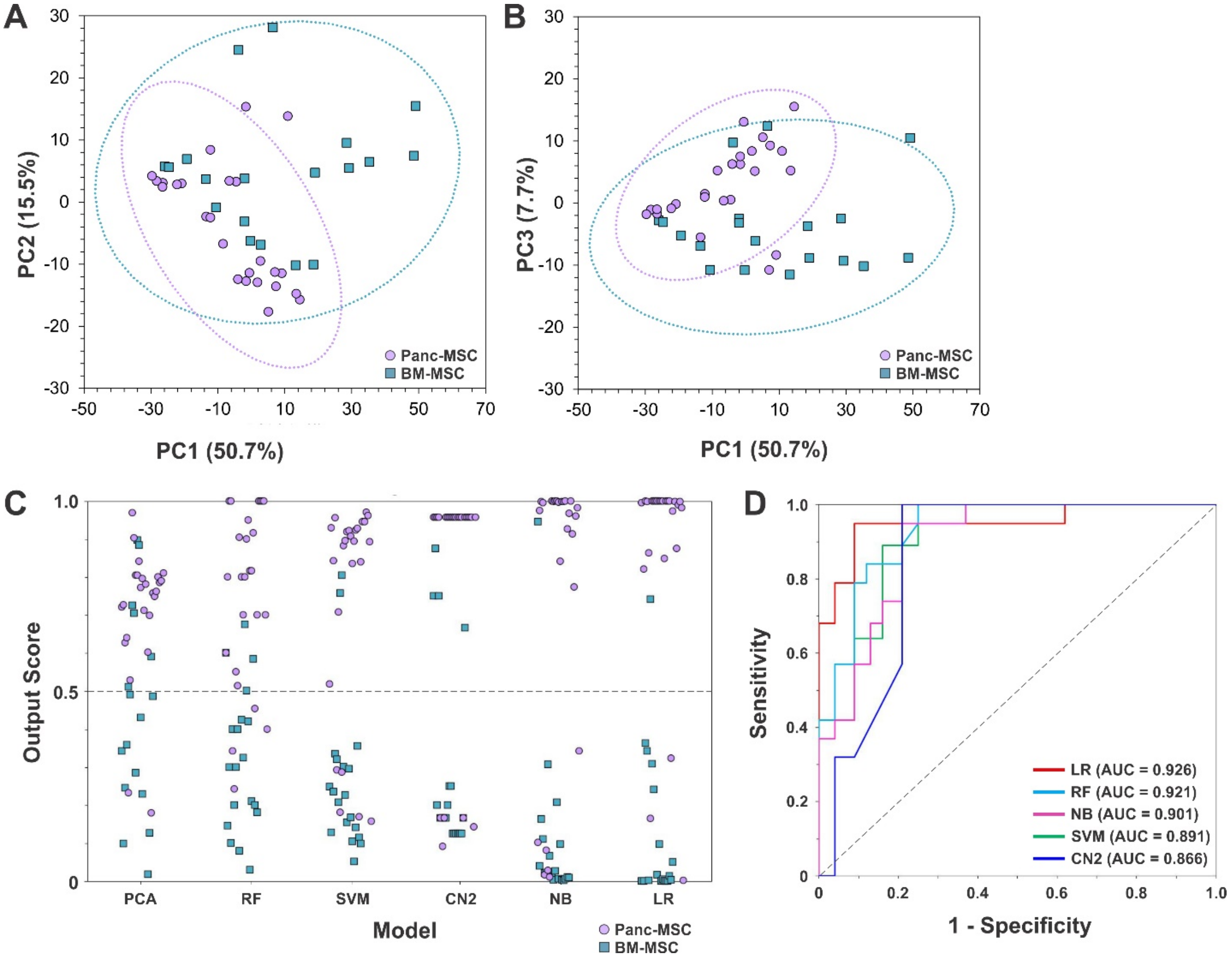

Fig. 6 PCA score plots of Panc-MSC and BM-MSC clusters constructed with the first and second PCs **(A)** and the first and third PCs **(B)**, where one data point corresponds to one SERS spectrum; comparison of final output scores of data given by PCA only (PC1 *vs.* PC3) and five machine learning algorithms **(C)**, where one data point corresponds to one SERS spectrum; ROC curves comparing various machine learning algorithms **(D)**

Table 3 Comparison of abilities of PCA and various machine learning algorithms to discriminate BM-MSC and Panc-MSC EVs based on SERS spectra

Model	Sensitivity	Specificity	Accuracy
PCA Only (PC1 *vs.* PC3)	74 %	84 %	82 %

Logistic Regression	89 %	88 %	89 %
Support Vector Machine	89 %	80 %	84 %
Random Forest	84 %	84 %	84 %
Naïve Bayes	95 %	76 %	84 %
CN2 Rule Induction	79 %	80 %	80 %

In terms of differentiating MSC-derived EVs from different sources, our model works comparatively well with respect to other published studies. Gualerzi *et al.* previously differentiated BM-MSC EVs from adipose tissue-derived MSC EVs and EVs released by dermal fibroblasts by conventional Raman spectroscopy [49]. In this study, PCA in conjunction with linear discriminant analysis (LDA) was used for EV classification, and an accuracy of 93.7 % was achieved. Although this accuracy is higher than that achieved by our PCA-LR model, it is important to note that the spectra collected by Gualerzi *et al.* had to undergo significant treatment prior to data analysis to remove autofluorescence and background induced by their 532 nm laser. The use of a SERS platform and a lower energy excitation wavelength (i.e., 785 nm) usually removes the need for significant data treatment for better peak resolution, as demonstrated by the spectra we obtained in this study (**Fig. 5**) and highly simplifies the data analysis.

Conclusion

Plasmonically active nanohole arrays were used to trap single EVs isolated from Panc- and BM-MSCs, which were subsequently analyzed by SERS. Although the nanohole arrays are plasmonically active in the red and near-infrared wavelength regions, we determined that the near-infrared (785 nm) laser was the most suitable for probing these biological samples. By irradiating both Panc-MSC and BM-MSC EVs with the 785 nm laser, we found that the SERS spectra for both groups contained predominantly protein peaks, as we would expect to find on EV membrane surfaces, as well as some nucleic acid peaks. PCA was employed to determine the main compositional differences between these two EV sources. We determined that the peaks responsible for most variance were located at 1236 cm^{-1}, corresponding to amide III, 761 cm^{-1}, belonging to tryptophan, and 1528 cm^{-1}, corresponding to in-plane -C=C- vibrations. PC scores were then used as simple classifiers in training machine learning algorithms to separate the Panc- and BM-MSC EVs. Using simpler classifiers instead of entire spectral data sets lower the computational demand and time required to complete this classification task. With a logistic regression machine learning algorithm, we were able to distinguish between the two EV types with 89 % accuracy, 89 % sensitivity, and 88 % specificity. In future work, we would like to challenge these platforms with cancer-derived EVs to explore their feasibility as a tool in disease detection and diagnosis.

Declarations

Conflicts of interests/Competing interests

The authors declare no known competing financial or non-financial interests.

Acknowledgements and funding information

The authors would like to gratefully thank the Nanofabrication Facility at the University of Western Ontario (Western University) for their assistance with the preparation of the platforms by electron-beam lithography. This research was supported by the Natural Sciences and Engineering Research Council (NSERC) of Canada (DG RGPIN-2020-06676).

References

1. Lawson C, Vicencio JM, Yellon DM, Davidson SM. Microvesicles and exosomes: New players in metabolic and cardiovascular disease. J Endocrinol. 2016;228(2):R57-71.

2. Veziroglu EM, Mias GI. Characterizing extracellular vesicles and their diverse RNA contents. Front Genet. 2020;11:700.

3. Shpacovitch V, Hergenröder R. Optical and surface plasmonic approaches to characterize extracellular vesicles. A review. Anal Chim Acta. 2018;1005:1-15.

4. Ståhl A-l, Johansson K, Mossberg M, Kahn R, Karpman D. Exosomes and microvesicles in normal physiology, pathophysiology, and renal diseases. Pediatr Nephrol. 2019;34(1):11-30.

5. Raposo G, Stoorvogel W. Extracellular vesicles: Exosomes, microvesicles, and friends. J Cell Biol. 2013;200(4):373-83.

6. Margolis L, Sadovsky Y. The biology of extracellular vesicles: The known unknowns. PLoS Biol. 2019;17(7):e3000363.

7. Pang B, Zhu Y, Ni J, Thompson J, Malouf D, Bucci J, et al. Extracellular vesicles: The next generation of biomarkers for liquid biopsy-based prostate cancer diagnosis. Theranostics. 2020;10(5):2309-26.

8. Mathew M, Zade M, Mezghani N, Patel R, Wang Y, Momen-Heravi F. Extracellular vesicles as biomarkers in cancer immunotherapy. Cancers (Basel). 2020;12(10):2825.

9. De Jong OG, Van Balkom BWM, Schiffelers RM, Bouten CVC, Verhaar MC. Extracellular vesicles: Potential roles in regenerative medicine. Front Immunol. 2014;5:608.

10. Marote A, Teixeira FG, Mendes-Pinheiro B, Salgado AJ. MSCs-derived exosomes: Cell-secreted nanovesicles with regenerative potential. Front Pharmacol. 2016;7:231.

11. Jing H, He X, Zheng J. Exosomes and regenerative medicine: State of the art and perspectives. Transl Res. 2018;196:1-16.

12. Xin H, Li Y, Buller B, Katakowski M, Zhang Y, Wang X, et al. Exosome-mediated transfer of mir-133b from multipotent mesenchymal stromal cells to neural cells contributes to neurite outgrowth. Stem Cells. 2012;30(7):1556-64.

13. Takeda YS, Xu Q. Neuronal differentiation of human mesenchymal stem cells using exosomes derived from differentiating neuronal cells. PLoS ONE. 2015;10(8):e0135111.

14. El Bassit G, Patel RS, Carter G, Shibu V, Patel AA, Song S, et al. E MALAT1 in human adipose stem cells modulates survival and alternative splicing of PKCdII in HT22 cells. Endocrinology. 2017;158(1):183-95.

15. Ibrahim Ahmed G-E, Cheng K, Marbán E. Exosomes as critical agents of cardiac regeneration triggered by cell therapy. Stem Cell Rep. 2014;2(5):606-19.

16. Zhao Y, Sun X, Cao W, Ma J, Sun L, Qian H, et al. Exosomes derived from human umbilical cord mesenchymal stem cells relieve acute myocardial ischemic injury. Stem Cells Int. 2015;2015:761643.

17. Agarwal U, George A, Bhutani S, Ghosh-Choudhary S, Maxwell JT, Brown ME, et al. Experimental, systems, and computational approaches to understanding the microRNA-mediated reparative potential of cardiac progenitor cell-derived exosomes from pediatric patients. Circ Res. 2017;120(4):701-12.

18. Tan CY, Lai RC, Wong W, Dan YY, Lim SK, Ho HK. Mesenchymal stem cell-derived exosomes promote hepatic regeneration in drug-induced liver injury models. Stem Cell Res Ther. 2014;5(3):76.

19. Nojima H, Freeman CM, Schuster RM, Japtok L, Kleuser B, Edwards MJ, et al. Hepatocyte exosomes mediate liver repair and regeneration via sphingosine-1-phosphate. J Hepatol. 2016;64(1):60-8.

20. Borges FT, Melo SA, Özdemir BC, Kato N, Revuelta I, Miller CA, et al. TGF-β1-containing exosomes from injured epithelial cells activate fibroblasts to initiate tissue regenerative responses and fibrosis. J Am Soc Nephrol. 2013;24(3):385-92.

21. Zhou Y, Xu H, Xu W, Wang B, Wu H, Tao Y, et al. Exosomes released by human umbilical cord mesenchymal stem cells protect against cisplatin-induced renal oxidative stress and apoptosis in vivo and in vitro. Stem Cell Res Ther. 2013;4(2):34.

22. Jiang ZZ, Liu YM, Niu X, Yin JY, Hu B, Guo SC, et al. Exosomes secreted by human urine-derived stem cells could prevent kidney complications from type I diabetes in rats. Stem Cell Res Ther. 2016;7:24.

23. Zhang J, Chen C, Hu B, Niu X, Liu X, Zhang G, et al. Exosomes derived from human endothelial progenitor cells accelerate cutaneous wound healing by promoting angiogenesis through erk1/2 signaling. Int J Biol Sci. 2016;12(12):1472-87.

24. Li X, Liu L, Yang J, Yu Y, Chai J, Wang L, et al. Exosome derived from human umbilical cord mesenchymal stem cell mediates miR-181c attenuating burn-induced excessive inflammation. EBioMedicine. 2016;8:72-82.

25. Zhao B, Zhang Y, Han S, Zhang W, Zhou Q, Guan H, et al. Exosomes derived from human amniotic epithelial cells accelerate wound healing and inhibit scar formation. J Mol Histol. 2017;48(2):121-32.

26. Furuta T, Miyaki S, Ishitobi H, Ogura T, Kato Y, Kamei N, et al. Mesenchymal stem cell-derived exosomes promote fracture healing in a mouse model. Stem Cells Transl Med. 2016;5(12):1620-30.

27. Qi X, Zhang J, Yuan H, Xu Z, Li Q, Niu X, et al. Exosomes secreted by human-induced pluripotent stem cell-derived mesenchymal stem cells repair critical-sized bone defects through enhanced angiogenesis and osteogenesis in osteoporotic rats. Int J Biol Sci. 2016;12(7):836-49.

28. Zhang S, Chu WC, Lai RC, Lim SK, Hui JHP, Toh WS. Exosomes derived from human embryonic mesenchymal stem cells promote osteochondral regeneration. Osteoarthr Cartil. 2016;24(12):2135-40.

29. Zhu Y, Wang Y, Zhao B, Niu X, Hu B, Li Q, et al. Comparison of exosomes secreted by induced pluripotent stem cell-derived mesenchymal stem cells and synovial membrane-derived mesenchymal stem cells for the treatment of osteoarthritis. Stem Cell Res Ther. 2017;8(1):64.

30. Nakamura Y, Miyaki S, Ishitobi H, Matsuyama S, Nakasa T, Kamei N, et al. Mesenchymal-stem-cell-derived exosomes accelerate skeletal muscle regeneration. FEBS Lett. 2015;589(11):1257-65.

31. Choi JS, Yoon HI, Lee KS, Choi YC, Yang SH, Kim I-S, et al. Exosomes from differentiating human skeletal muscle cells trigger myogenesis of stem cells and provide biochemical cues for skeletal muscle regeneration. J Control Release. 2016;222:107-15.

32. Zhang Y, Chopp M, Zhang ZG, Katakowski M, Xin H, Qu C, et al. Systemic administration of cell-free exosomes generated by human bone marrow derived mesenchymal stem cells cultured under 2D and 3D conditions improves functional recovery in rats after traumatic brain injury. Neurochem Int. 2017;111:69-81.

33. Mead B, Tomarev S. Bone marrow-derived mesenchymal stem cells-derived exosomes promote survival of retinal ganglion cells through mirna-dependent mechanisms. Stem Cells Transl Med. 2017;6(4):1273-85.

34. Teng X, Chen L, Chen W, Yang J, Yang Z, Shen Z. Mesenchymal stem cell-derived exosomes improve the microenvironment of infarcted myocardium contributing to angiogenesis and anti-inflammation. Cell Physiol Biochem. 2015;37(6):2415-24.

35. Tomasoni S, Longaretti L, Rota C, Morigi M, Conti S, Gotti E, et al. Transfer of growth factor receptor mRNA via exosomes unravels the regenerative effect of mesenchymal stem cells. Stem Cells Dev. 2013;22(5):772-80.

36. van Niel G, D'Angelo G, Raposo G. Shedding light on the cell biology of extracellular vesicles. Nat Rev Mol Cell Biol. 2018;19(4):213-28.

37. Möller A, Lobb RJ. The evolving translational potential of small extracellular vesicles in cancer. Nat Rev Cancer. 2020;20(12):697-709.

38. Moskovits M. Persistent misconceptions regarding SERS. Phys Chem Chem Phys. 2013;15(15):5301-11.

39. Rojalin T, Phong B, Koster HJ, Carney RP. Nanoplasmonic approaches for sensitive detection and molecular characterization of extracellular vesicles. Front Chem. 2019;7:279.

40. Iliescu FS, Vrtačnik D, Neuzil P, Iliescu C. Microfluidic technology for clinical applications of exosomes. Micromachines. 2019;10(6):392.

41. Zong S, Wang L, Chen C, Lu J, Zhu D, Zhang Y, et al. Facile detection of tumor-derived exosomes using magnetic nanobeads and SERS nanoprobes. Anal Methods. 2016;8(25):5001-8.

42. Tian YF, Ning CF, He F, Yin BC, Ye BC. Highly sensitive detection of exosomes by SERS using gold nanostar@Raman reporter@nanoshell structures modified with a bivalent cholesterol-labeled DNA anchor. Analyst. 2018;143(20):4915-22.

43. Beekman P, Enciso-Martinez A, Rho HS, Pujari SP, Lenferink A, Zuilhof H, et al. Immuno-capture of extracellular vesicles for individual multi-modal characterization using AFM, SEM and Raman spectroscopy. Lab Chip. 2019;19(15):2526-36.

44. Kwizera EA, O'Connor R, Vinduska V, Williams M, Butch ER, Snyder SE, et al. Molecular detection and analysis of exosomes using surface-enhanced Raman scattering gold nanorods and a miniaturized device. Theranostics. 2018;8(10):2722-38.

45. Kim N, Thomas MR, Bergholt MS, Pence IJ, Seong H, Charchar P, et al. Surface enhanced Raman scattering artificial nose for high dimensionality fingerprinting. Nat Commun. 2020;11(1):207.

46. Lee C, Carney RP, Hazari S, Smith ZJ, Knudson A, Robertson CS, et al. 3D plasmonic nanobowl platform for the study of exosomes in solution. Nanoscale. 2015;7(20):9290-7.

47. Sivashanmugan K, Huang W-L, Lin C-H, Liao J-D, Lin C-C, Su W-C, et al. Bimetallic nanoplasmonic gap-mode SERS substrate for lung normal and cancer-derived exosomes detection. J Taiwan Inst Chem Eng. 2017;80:149-55.

48. Yan Z, Dutta S, Liu Z, Yu X, Mesgarzadeh N, Ji F, et al. A label-free platform for identification of exosomes from different sources. ACS Sens. 2019;4(2):488-97.

49. Gualerzi A, Niada S, Giannasi C, Picciolini S, Morasso C, Vanna R, et al. Raman spectroscopy uncovers biochemical tissue-related features of extracellular vesicles from mesenchymal stromal cells. Sci Rep. 2017;7(1):9820.

50. Gualerzi A, Kooijmans SAA, Niada S, Picciolini S, Brini AT, Camussi G, et al. Raman spectroscopy as a quick tool to assess purity of extracellular vesicle preparations and predict their functionality. J Extracell Vesicles. 2019;8(1):1568780.

51. Kaufman L, Cooper T, Wallace G, Hawke D, Betts D, Hess D, et al. Trapping and SERS identification of extracellular vesicles using nanohole arrays. Proc SPIE 10894: Plasmonics in Biology and Medicine XVI, 108940B; 2019.

52. Sherman SE, Kuljanin M, Cooper TT, Putman DM, Lajoie GA, Hess DA. High aldehyde dehydrogenase activity identifies a subset of human mesenchymal stromal cells with vascular regenerative potential. Stem Cells. 2017;35(6):1542-53.

53. Cooper TT, Sherman SE, Bell GI, Ma J, Kuljanin M, Jose SE, et al. Characterization of a vimentin^{high}/nestin^{high} proteome and tissue regenerative secretome generated by human pancreas-derived mesenchymal stromal cells. Stem Cells. 2020;38(5):666-82.

54. Cooper TT, Sherman SE, Bell GI, Dayarathna T, McRae DM, Ma J, et al. Ultrafiltration and injection of islet regenerative stimuli secreted by pancreatic mesenchymal stromal cells. Stem Cells Dev. 2021;30(5):247-64.

55. Haynes CL, McFarland AD, Van Duyne RP. Surface-enhanced Raman spectroscopy. Anal Chem. 2005;77(17):338 A-46 A.

56. Sur UK. Surface-enhanced Raman spectroscopy. Resonance. 2010;15(2):154-64.

57. Guo L, Jackman JA, Yang H-H, Chen P, Cho N-J, Kim D-H. Strategies for enhancing the sensitivity of plasmonic nanosensors. Nano Today. 2015;10(2):213-39.

58. Talari ACS, Movasaghi Z, Rehman S, Rehman IU. Raman spectroscopy of biological tissues. Appl Spectrosc Rev. 2015;50(1):46-111.

59. Rehman IU, Movasaghi Z, Rehman S. FTIR and Raman characteristic peak frequencies in biological studies. Vibrational spectroscopy for tissue analysis. 1. Boca Raton: CRC Press; 2012. p. 213-94.

60. Stremersch S, Marro M, Pinchasik B-E, Baatsen P, Hendrix A, De Smedt SC, et al. Identification of individual exosome-like vesicles by surface enhanced Raman spectroscopy. Small. 2016;12(24):3292-301.

61. Rau KR, Guerra A, Vogel A, Venugopalan V. Investigation of laser-induced cell lysis using time-resolved imaging. Appl Phys Lett. 2004;84(15):2940-2.

62. Gazor M, Talesh SSA, kavianpour A, Khatami M, Javidanbardan A, Hosseini SN. A novel cell disruption approach: Effectiveness of laser-induced cell lysis of pichia pastoris in the continuous system. Biotechnol Bioproc E. 2018;23(1):49-54.

63. Huang Z, McWilliams A, Lui H, McLean DI, Lam S, Zeng H. Near-infrared Raman spectroscopy for optical diagnosis of lung cancer. Int J Cancer. 2003;107(6):1047-52.

64. Shin H, Oh S, Hong S, Kang M, Kang D, Ji Y-g, et al. Early-stage lung cancer diagnosis by deep learning-based spectroscopic analysis of circulating exosomes. ACS Nano. 2020;14(5):5435-44.

65. Howley T, Madden MG, O'Connell M-L, Ryder AG. The effect of principal component analysis on machine learning accuracy with high dimensional spectral data. Proc AI-2005: Applications and Innovcations in Intelligent Systems XII; 2005. p. 209-22.

66. Qi Y. Random forest for bioinformatics. In: Zhang C, Ma Y, editors. Ensemble machine learning: Methods and applications. Boston, MA: Springer US; 2012. p. 307-23.

67. Binkhonain M, Zhao L. A review of machine learning algorithms for identification and classification of non-functional requirements. Expert Syst Appl. 2019;1:100001.

68. Swe SM, Sett KM. Approaching rules induction CN2 algorithm in categorizing of biodiversity. Int J Trend Sci Res Dev. 2019;3(4):1581-4.

69. Dreiseitl S, Ohno-Machado L. Logistic regression and artificial neural network classification models: A methodology review. J Biomed Inform. 2002;35(5):352-9.